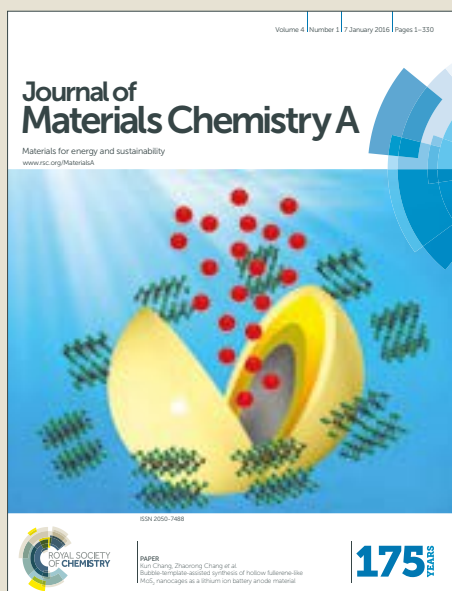


Journal of Materials Chemistry A

Accepted Manuscript



This article can be cited before page numbers have been issued, to do this please use: W. Greenbank, N. J. Rolston, E. Destouesse, G. Wantz, L. Hirsch, R. H. Dauskardt and S. Chambon, *J. Mater. Chem. A*, 2017, DOI: 10.1039/C6TA09665D.



This is an Accepted Manuscript, which has been through the Royal Society of Chemistry peer review process and has been accepted for publication.

Accepted Manuscripts are published online shortly after acceptance, before technical editing, formatting and proof reading. Using this free service, authors can make their results available to the community, in citable form, before we publish the edited article. We will replace this Accepted Manuscript with the edited and formatted Advance Article as soon as it is available.

You can find more information about Accepted Manuscripts in the [author guidelines](#).

Please note that technical editing may introduce minor changes to the text and/or graphics, which may alter content. The journal's standard [Terms & Conditions](#) and the ethical guidelines, outlined in our [author and reviewer resource centre](#), still apply. In no event shall the Royal Society of Chemistry be held responsible for any errors or omissions in this Accepted Manuscript or any consequences arising from the use of any information it contains.

ARTICLE

Improved mechanical adhesion and electronic stability of organic solar cells with thermal ageing: the role of diffusion at the hole extraction interface

W. Greenbank,^a N. Rolston,^b E. Destouesse,^a G. Wantz,^a L. Hirsch,^a R. Dauskardt^c and S. Chambon^a

Received 00th January 20xx,
Accepted 00th January 20xx

DOI: 10.1039/x0xx00000x

www.rsc.org/

Organic photovoltaic (OPV) solar cells are a promising option for cheap, renewable energy, but must improve in their stability. This study examines changes in the IV parameters of inverted OPV devices with thermal ageing, and correlates them to changes in the mechanical stability of the devices observed by fracture analysis. In particular, the role that the use of different materials in the hole transport layer (HTL) and metal electrode has in determining the stability (both mechanical and electronic) of the device is studied. Data from a range of characterization techniques (including Kelvin probe analysis and X-ray photoelectron spectroscopy elemental depth profiling) are used to correlate changes in device structure and performance, demonstrating the presence of inter-layer diffusion when silver is used as an electrode material. This inter-diffusion has the beneficial effect of improving the adhesion of the electrode to the device, but is correlated to declines in the performance of the device when used in conjunction with MoO₃ as an HTL. An improvement in adhesion is also seen with aluminium electrodes, but without any signs of diffusion, showing that an improvement in the mechanical stability of a device when thermally aged need not come at the expense of performance stability.

Introduction

Organic photovoltaic (OPV) solar cells are a third generation photovoltaic technology that represent a promising zero-emission power source for confronting the dual challenges of anthropogenic climate change and increased global demand for energy. Their appeal lies in their very low production cost (mostly arising from having no requirement for high temperatures or extreme sensitivity to impurities) as compared to their more expensive inorganic counterparts.¹ These properties mean that they have energy payback times on the order of months, rather than the years for inorganic PV technology.² Polymer-based OPV solar cells have rapidly improved in efficiency since their invention 30 years ago^{1,3} to reach a record power conversion efficiency (PCE) of 11.7%.⁴ While much lower than inorganic devices,⁵ the price advantage is such that commercialisation of OPV is being extensively pursued.^{6,7} However, OPV devices are still plagued by short lifetimes,⁸ which limits their commercial applicability. The mechanisms which give rise to PCE loss in OPV are

complex, and not yet fully understood. OPV are vulnerable to four principal ageing stimuli: heat, light, oxygen and water. Each of these stimuli can attack the device at different points in its structure, inhibiting: exciton formation, diffusion, and separation; charge migration; and charge extraction.⁹ One particular vulnerability in standard, “direct”, devices (in which hole extraction occurs at the transparent electrode, and electron extraction occurs at the metal electrode) is the use of low work function metals, such as calcium. These metals are easily corroded by water and oxygen, forming insulating oxides that reduce the active area of the device.^{10,11} To combat this, the inverted structure was developed,^{12–14} in which holes are extracted via the metal electrode and electrons via the transparent electrode, enabling the use of more environmentally-stable metal oxides as the hole and electron transport layers.

In recent studies, the specific influence of the HTL on the degradation mechanisms has been investigated.^{15,16} In particular, we demonstrated that the use of certain metal oxides as hole transport layers (HTLs) can give rise to interfacial thermal degradation at the hole extraction interface.¹⁵ In particular, we observed that the use of molybdenum oxide as a hole transport layer, in conjunction with a silver electrode, gave rise to an open-circuit voltage (V_{oc})-driven degradation mechanism which was specific to this combination of materials. In addition, using atomic force microscopy (AFM) and Rutherford backscattering spectrometry (RBS), we observed a significant increase in the roughness of the morphology of devices that use silver as an electrode material. We concluded

^a University of Bordeaux, CNRS, Bordeaux INP, IMS, UMR 5218 Talence, 33405 (France).

^b Department of Applied Physics, Stanford University Stanford, California, 94305-4034 (United States of America).

^c Department of Materials Science and Engineering, Stanford University Stanford, California, 94305-4034 (United States of America).

† Footnotes relating to the title and/or authors should appear here.

Electronic Supplementary Information (ESI) available: [details of any supplementary information available should be included here]. See DOI: 10.1039/x0xx00000x

that such behaviour would be consistent with a de-wetting or delamination mechanism, and that of the four material combinations examined, the use of WO_3 as an HTL and aluminium as an electrode provided the highest stability with thermal ageing.¹⁵

Adhesion is the interface resistance to mechanical separation for two materials. Most traditional adhesion measurement methods, such as the scratch and peel test, are qualitative in nature and lack reproducibility. In order to quantify the adhesion of an interface, the theories of fracture mechanics can be applied by bonding the materials of interest between two thick beams. When applying loads to the beams, the beams bend and store up elastic energy. A crack begins to propagate once a critical load is reached, and the resulting relaxation in strain energy provides a driving force for fracture.

We used a double cantilever beam (DCB) sample geometry to determine interlayer adhesion, where the ends of a sample were pulled apart with a uniaxial load. The force applied and displacement of the beam edges were measured in the test. The loading system comprised a stiff load frame, an actuator that can measure displacements with a resolution of 1 nm, and a load cell. Linear elastic fracture mechanics theory was used to calculate the strain energy release rate, which corresponds to the value of interfacial adhesion.¹⁷

The purpose of this study was to combine both electronic and mechanical characterisation techniques to examine the effects of thermal ageing on the mechanical stability of the hole extraction interface in inverted OPV solar cells. By examining the evolution of the fracture energy of the devices with thermal ageing, our aim was to understand how the choice of particular materials can influence the resilience of a device to thermal stress, and therefore how device design can enhance interfacial stability. To do this, devices incorporating MoO_3 or WO_3 as HTLs and aluminium or silver as metal electrodes were fabricated and aged in the dark at 85°C under inert atmosphere following the ISOS-D2 protocol (high temperature storage in the dark).¹⁸ By excluding other ageing stimuli, this enabled the effects of heat on interfacial stability to be examined in isolation, which is instructive because these effects will be observed in any commercial application of OPV, whether or not mitigation strategies like encapsulation or UV filtering are used. The aged devices were made into adhesion specimens to determine their fracture energy, and the fractured samples were analysed by X-ray photoelectron spectrometry (XPS) to determine the fracture path in the sample and Kelvin probe analysis to monitor changes in the work function of the interface. XPS was also used, in conjunction with argon etching to monitor changes in the elemental profile of the fractured samples with depth.

Experimental

The samples for mechanical testing were prepared on glass substrates (Paul Marienfeld GmbH, Germany) measuring 56 mm × 72 mm. They were prepared without a conductive transparent electrode, as it was not necessary for the fracture testing. The ZnO layer was deposited via doctor blade coating from a sol-gel, prepared as follows: zinc acetate dihydrate

(Sigma-Aldrich) was dissolved in butanol at a concentration of 0.18 mol L⁻¹, to which ethanolamine was added to give a molar ratio (ethanolamine/ $\text{Zn}(\text{OAc})_2$) of 0.45. The solution was stirred in three stages: at 60°C for one hour, at 80°C for one hour, and then at room temperature for 48 hours. Finally, the solution was diluted by a factor of two before use. Deposition was carried out at a speed of 10 mm s⁻¹, with a blade height of 12 μm, a solution volume of 20 μL and a temperature of 50°C. The coated samples were subsequently annealed at 140°C for one minute. The resulting layers of ZnO were measured by mechanical profilometry, and were found to be between 30 nm and 40 nm thick. The bulk heterojunction (BHJ) was a 1:1 w/w blend of poly(3-hexylthiophene) (P3HT) and [6,6]-phenyl-C₆₁-butyric acid methyl ester (PCBM). The BHJ was deposited by doctor blade coating from a solution that was 30 mg mL⁻¹ P3HT (Plextronics Plexcore OS2100, 53 kDa) and 30 mg mL⁻¹ PCBM (Solaris Chem.) in chlorobenzene, using: 45 μL of the solution per substrate, a blade height of 250 μm, a temperature of 70°C, and coating speed of 30 mm s⁻¹. The samples were subsequently annealed in 1,2-dichlorobenzene vapour. The thickness of the BHJ layer was found to be 183 ± 11 nm, measured by mechanical profilometry. Following this step during fabrication and ageing, the samples were kept under inert atmosphere in a glovebox (N₂ atmosphere, <0.1 ppm O₂, H₂O). The hole transport and metal electrode layers were deposited by electron-beam and thermal evaporation respectively. Their thicknesses were 10 nm and 80 nm respectively.

The samples were aged on a hotplate, in the dark in an inert atmosphere in a glovebox. Following ageing, they were stored and transported between France and the United States in the dark under the same inert atmosphere.

The preparation, measurement, and ageing of the inverted P3HT:PC₆₁BM OPV samples for IV characterisation is detailed in a previous study.¹⁵ The devices' architecture is glass/ITO/ZnO/P3HT:PC₆₁BM/(MoO_3 or WO_3)/(Al or Ag) with a 10 mm² device area. The inverted poly(carbazole-dithiophene-benzothiadiazole):[6,6]-phenyl-C₇₁-butyric acid methyl ester (PCDTBT:PC₇₁BM) OPV samples had the structure glass/ITO/ZnO/PCDTBT:PC₇₁BM/ MoO_3 /(Al or Ag), and were prepared in the same way as was detailed in the previous study,¹⁵ with the exception of the BHJ active layer, which was prepared as follows. A solution was prepared by adding 10.5 mg of PCDTBT (St-Jean Photochemicals, M_w=125 kDa, PDI=5.2) and 29.4 mg of PC₇₁BM (Solaris Chem., >99%) to 2 mL of 1,2-dichlorobenzene (Sigma-Aldrich, >99%) in a glovebox under a nitrogen atmosphere and then stirring at 85°C for two days. Prior to deposition by spin-coating, a number of test samples were prepared to determine the optimal spin-coating speed to produce a 90 nm thick active layer. This was found to be 1270 RPM. The thickness was determined with a mechanical profilometer. Once the optimal speed was determined, all the samples were coated at 1270 RPM for 90 seconds. No further annealing of the active layer was required. The initial device performances and evolution of all PV parameters with thermal ageing are detailed in Table S1 and Figure S1 in the ESI.

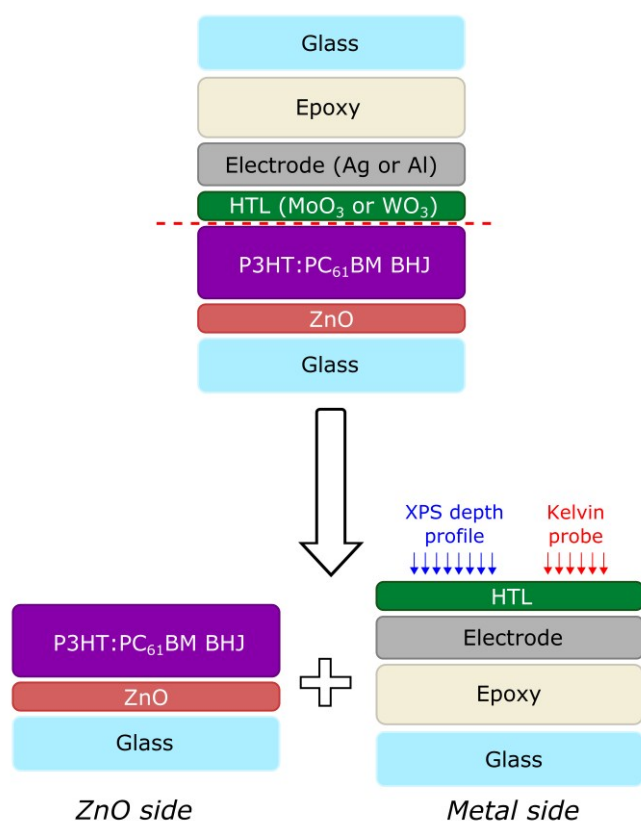


Figure 1: A schematic of a sample before and after a fracture experiment in which the sample fractures at the active layer/HTL interface (red dashed line). Samples that fractured at this interface were able to be analysed by XPS depth profiling and Kelvin probe, as depicted here.

Double cantilever beam (DCB) specimens were made with an additional glass beam bonded with room-temperature cured E-20NS Loctite epoxy on top of the OPV samples. The specimens were loaded under displacement control in a thin-film cohesion testing system (Delaminator DTS, Menlo Park, CA) from which a load, P , versus displacement, Δ , curve was recorded. The fracture energy, G_C (J m^{-2}), was measured in terms of the critical value of the applied strain energy release rate, G . G_C can be expressed in terms of the critical load, P_C , at which crack growth occurs, the crack length, a , the plain strain elastic modulus, E' , of the substrates and the specimen dimensions; width, b and half-thickness, h . G_C was calculated from equation (1):¹⁹

$$G_C = \frac{12P_C^2 a^2}{B^2 E' h^3} \left(1 + 0.64 \frac{h}{a}\right)^2 \quad (1)$$

An estimate of the crack length was experimentally obtained from a measurement of the elastic compliance, $d\Delta/dP$, using the compliance relationship in equation (2):

$$a = \left(\frac{d\Delta}{dP} \times \frac{BE'h^3}{8}\right)^{1/3} - 0.64h \quad (2)$$

All G_C testing was performed in a standard laboratory air environment at $\sim 25^\circ\text{C}$ and $\sim 40\%$ R.H.

Following fracture testing, a survey X-ray photoelectron spectroscopy (XPS, PHI 5000 Versaprobe) scan (0 – 1100 eV) was made of each of the fractured specimens using monochromatic Al K_α X-ray radiation at 1487 eV in order to

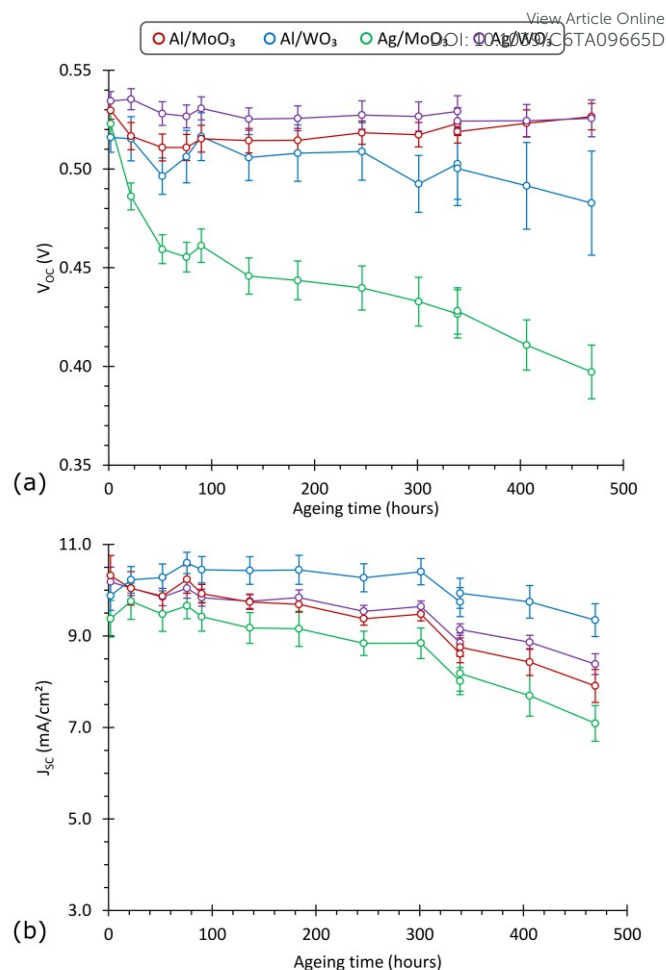


Figure 2: Evolution of (a) the V_{OC} and (b) the J_{SC} with thermal ageing of inverted P3HT:PCBM devices with various top electrode/HTL combinations. The devices were aged at 85°C in the dark under an inert atmosphere. Uncertainties represent one standard deviation when averaged across 16 devices.

characterize the surface chemistry and to help precisely locate the failure path. In addition, depth profiling was performed to quantify interfacial diffusion after ageing. An X-ray beam spot of $200\ \mu\text{m} \times 200\ \mu\text{m}$ with a detection angle of 35° was used with a beam of Ar^+ ions to etch the sample surface, rastered over an area of $2\ \text{mm} \times 2\ \text{mm}$ with a beam current of $0.5\ \mu\text{A}$ and voltage of $1\ \text{kV}$. Scans were taken every 30 s to determine the atomic concentration of each element in the sample at a given depth. The specimen half containing the metal electrode is referred to as the “metal side”, and the other half including the ZnO is referred to as the “ZnO side” (Figure 1). Detailed high-resolution XPS scans were made for compositional analysis and further identification of the fracture path. Atomic force microscopy (AFM) (XE-70, Park Systems) in tapping mode was used to characterize the surface morphology and roughness of the fracture path. In addition, phase images were simultaneously collected to reveal further material properties and variations in the surface properties of the fractured cells.

Kelvin probe analysis was carried out on the metal side of samples that fractured at the BHJ/HTL interface using a

scanning Kelvin probe (KP Technology Model 5050). All measurements were calibrated to a specimen of highly oriented pyrolytic graphite (HOPG) with a work function of 4.65 eV.^{20,21}

Results and Discussion

Photovoltaic performances. In a previous study,¹⁵ we have studied the role that the materials used in the top electrode/HTL have in determining the resilience of inverted OPV devices to thermal ageing at 85°C. The evolution of the PV parameters with thermal degradation of four different architectures (Al/MoO₃, Al/WO₃, Ag/MoO₃, and Ag/WO₃) was studied. Initially, the samples all exhibit similar PV performances, with an average PCE between 3.18 and 3.54% (See Table S2 and Figure S2 in the ESI). Two kinds of degradation mechanisms were identified with thermal ageing. The first, observed with all four architectures, is a decline in short-circuit current density (J_{SC}) (Figure 2b). This degradation is typically attributed to morphological changes in the BHJ.²² Over time, the increased temperature accelerates phase segregation, leading to the growth of large donor (P3HT) and acceptor (PCBM) domains, increasing the rate of geminate recombination as the domain size exceeds the diffusion length of the photo-generated excitons.⁹ The second degradation mechanism observed is specific to samples containing MoO₃ HTLs and silver top electrodes. This mechanism is typified by a rapid loss of V_{OC} (Figure 2a) and FF in the first week of ageing, which is not observed in any other material combination. The physical origin of this degradation mechanism has yet to be demonstrated, but diffusion of species from the HTL or electrode into the active layer has been proposed as a possible mechanism.

Fracture Energy Analysis. In order to understand how material selection at the hole-extraction interface can influence the mechanical stability of the OPV samples to thermal ageing, a fracture analysis study of the four combinations of electrode/HTL materials in P3HT:PCBM OPV samples (Figure 1) with thermal ageing was carried out. The evolution of the fracture energy with thermal ageing is shown in Figure 3. The fracture path was determined by visual inspection, as the devices fracturing at the BHJ/HTL interface have metallic

appearance and those fracturing in the BHJ present a colour purple (See Figure S3 in the ESI). The samples that appeared (visually) to fracture at the HTL/BHJ interface were also analysed by XPS to confirm the fracture path (See Figures S4-S9 in the ESI). Initially, the samples all have relatively low values for fracture energy,^{23,24} between 1 J m⁻² and 2 J m⁻², and in all the samples the fracture occurs at the BHJ/HTL interface. These values are slightly higher than those recorded by Dupont et al. with similar OPV samples,²⁵ however this is most likely a result of the differences in processing conditions of the samples. After one week of thermal ageing, a rise in fracture energy occurs in all four architectures – a first indication of strengthening of the interfaces. In the case of the aluminium-containing samples, the fracture energy increases to over 3 J m⁻² and is accompanied by a shift in the fracture path, from the BHJ/HTL interface to inside the BHJ. The fracture no longer propagates via delamination of the top layers from the active layer but rather by decohesion of the active layer. This indicates that the adhesion at the HTL/BHJ interface in the aluminium-containing samples increased beyond the cohesion of the active layer. The fracture energy does not vary significantly with further ageing and the fracture path remains in the BHJ, indicating that the HTL/BHJ interfacial adhesion remains stronger than the aged BHJ itself.

The fracture energy in the silver-containing samples increased to between 2.3 J m⁻² and 2.6 J m⁻² after the first week of ageing, but the fracture path remained at the BHJ/HTL interface. This indicates that there has been an increase in adhesion of the top layers to the active layer in the silver-containing samples, and that if a decline in cohesion of the active layer has occurred, it was not by enough to cause a shift in the fracture path. Based on the fracture energies and paths of the two sets of samples, it is reasonable to conclude that the cohesion energy of the BHJ is somewhere between 2.6 J m⁻² and 3.0 J m⁻² after one week of thermal ageing. After two weeks of thermal ageing of the silver samples, the fracture path shifted to within the BHJ without exhibiting significant changes in the fracture energy (particularly in the Ag/WO₃ samples), which could be an indication of weakening of the BHJ. After three weeks ageing, the fracture energy and the fracture path do not vary further.

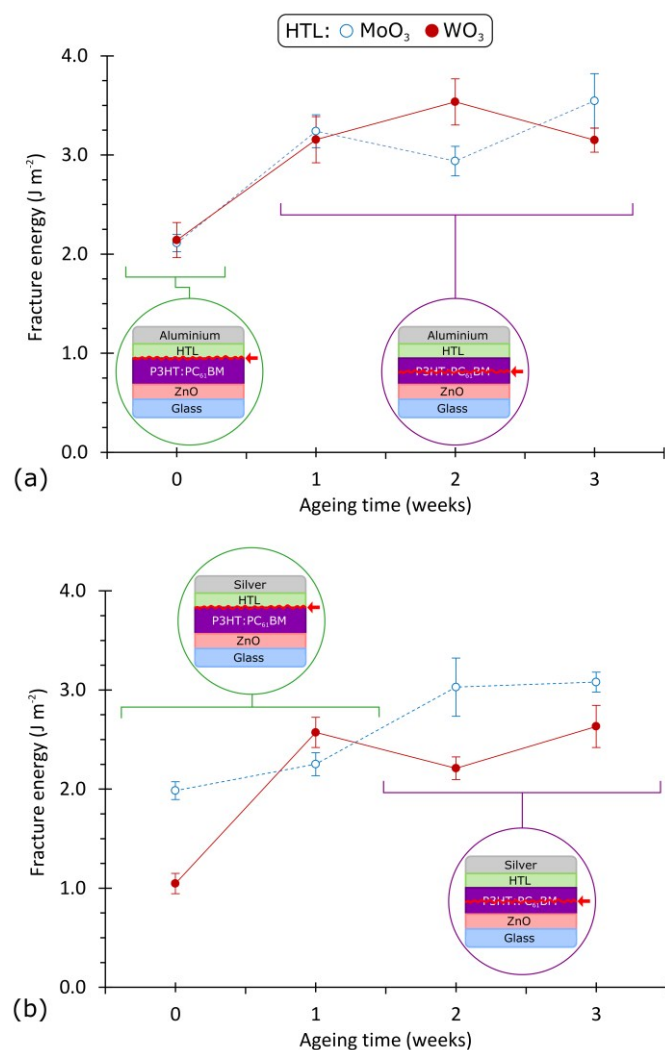


Figure 3: The measured G_c (J m^{-2}) of the aluminium (A) and silver (B) OPV samples with thermal ageing. Samples using WO_3 as an HTL are shown in red (solid line and full circle) and MoO_3 in blue (dashed line and hollow circle). The sample structures are shown in the insets, along with the the fracture paths (as determined by XPS – data given in supplementary information). Uncertainties represent standard error when averaged across 20–60 measurements.

These trends are particularly interesting with respect to the data

obtained from the Ag/ WO_3 samples. As the fracture path will migrate to the weakest point in a device from where it was initiated,²² the shift of the fracture path from the BHJ/HTL interface to within the BHJ between week 1 and week 2 with no change in the fracture energy indicates a decrease in the cohesion of the BHJ, i.e. at the end of week one the BHJ must have been stronger than at the end of week two. The timescale and prevalence of this BHJ weakening correlates to the J_{SC} loss observed in the PV devices for all the material combinations that were tested at the hole-collecting interface (Figure 2).¹⁵ With respect to mechanical stability, it has been shown previously that increased phase segregation with long-term exposure to elevated temperatures in the BHJ leads to crack propagation in the boundaries between P3HT-rich regions and PCBM-rich regions.^{23,26} In addition, it has been demonstrated previously that with a poly(3,4-ethylenedioxythiophene) polystyrene sulfonate (PEDOT:PSS) HTL and silver top electrode, annealing increases the entanglement at the HTL/BHJ interface and leads to fracture within the weaker fullerene-rich layer. The fullerenes act as defects within the polymer matrix for crack propagation.²⁷ It follows that phase segregation is likely the principle cause of BHJ weakening relative to the BHJ/HTL interface with long-term thermal ageing.

The aluminium and silver samples differ in their early fracture energy trends with thermal ageing. In both cases, the fracture energy increases with the first week of thermal ageing. In the case of the aluminium samples, this is accompanied by an immediate shift in the fracture path from the HTL/BHJ interface to within the BHJ, while, in the silver samples the fracture path does not shift to inside the BHJ until after two weeks ageing (Figure 3). After one week of thermal ageing the silver samples continue to fracture at the HTL/BHJ interface, despite the increase in fracture energy. It is evident that, with both electrodes, an increase in the adhesion of the electrode and HTL to the BHJ is occurring, but magnitude of the increase differs. This difference suggests that the increase in adhesion is related to the composition of the hole-extraction interface, and is not simply a result of bulk phenomena.

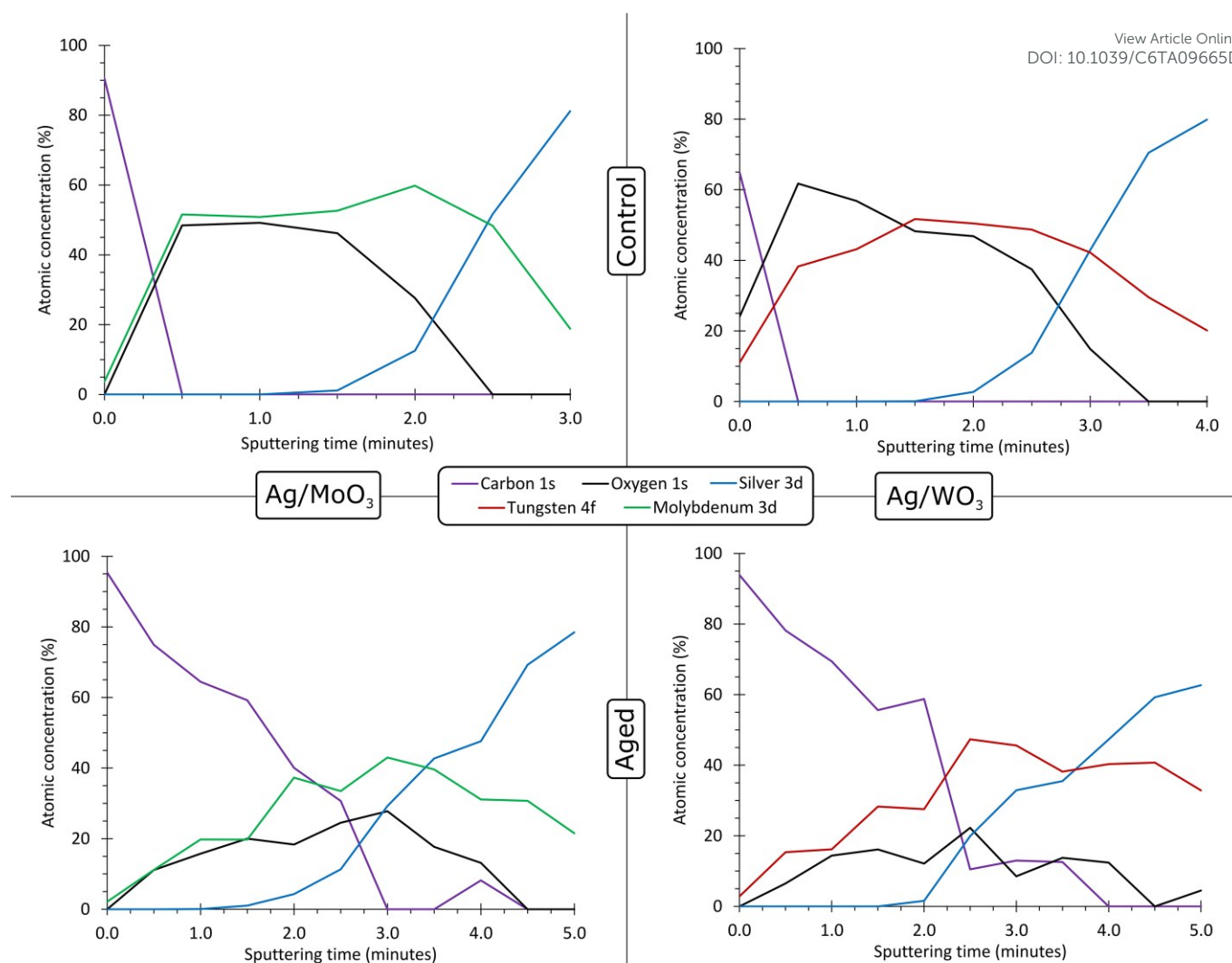


Figure 4: XPS depth profiles of the fractured unaged Ag/MoO₃ and Ag/WO₃ samples, and fractured samples that had been aged for one week at 85°C. In all cases the fracture plane was along the HTL/BHJ interface, and the metal side is analysed.

XPS elemental depth profiling. In order to understand the origins of the observed increases in adhesion at the hole-extraction interface, XPS depth profiling was performed on the metal side of the fractured samples to examine for the presence of inter-diffusion at the hole-collecting interface (Figure 4). It was only possible to examine samples that fractured at the interface, i.e. the silver-containing samples, as the thick layers of BHJ on the other samples obscured the interfacial properties. However, diffusion can be ruled out in the case of the aluminium-containing samples. In a previous study, we used Rutherford Backscattering Spectrometry (RBS) to examine samples with only HTL (MoO₃ or WO₃) and aluminium layers on glassy carbon substrates that underwent thermal ageing in the same conditions as in this study.¹⁵ The elemental profiles of the aluminium-containing samples showed no change with thermal ageing, indicating that aluminium does not diffuse through the HTL (MoO₃ or WO₃). Diffusion of species from the HTL into the active layer cannot be totally ruled out, however, as the samples in the RBS experiment were fabricated on glassy carbon substrates without a BHJ.

With respect to the fractured silver-containing samples analysed by XPS depth profiling, the control samples exhibit good segregation between the BHJ (carbon), the HTL (molybdenum/tungsten and oxygen) and the electrode (silver) as shown in Figure 4. At the interface between the HTL and the BHJ, there is very clear delineation between the carbon of the active layer, and the tungsten/molybdenum and oxygen of the HTL. The transition between the two takes place in the first 30 seconds of etching. At the silver/HTL interface the transition is more gradual; however this may be due to an etching artefact. After one week of thermal ageing, a significant change was observed at the interface. The previously well-segregated layers show a high degree of intermixing (Figure 4). In particular, the HTL elements are smeared over all of the sample depth that was analysed, and can still be detected after five or six minutes of sputtering. There doesn't appear to be any clear difference between the two HTLs in this respect. This is coupled with the concentration of carbon from the active declining much slower with depth, so much so that it intermixes with silver from the electrode. The silver concentration increases much more slowly with depth in the aged samples than was observed in the control

samples. As with the RBS studies performed on similar samples previously,¹⁵ such results could be a product of a change in the roughness of the sample. However, this is unlikely to be the case in this study, as the measurement is done of a fractured surface and the roughness is largely determined by the fracture path rather than changes during aging. In order to confirm this, AFM measurements were carried out on the fractured silver samples (un-aged and one week). These measurements showed an increase in surface roughness from ca. 1 nm to ca. 5 nm (data given in Figure S10 in the ESI), which would not be sufficient to explain the changes in the XPS depth profiles. It follows that the observed changes are a result of thermally-induced inter-diffusion between the layers at the hole-collecting interface, which is consistent with the increase in fracture energy observed in the first week of thermal ageing (Figure 3). It should be noted though that these observations only relate to thermal degradation. As observed by Corazza *et al.*, if other degradation stimuli are present, such as UV irradiation and/or humidity, diffusion and intermixing of the different layers can be amplified resulting in different fracture energy trends with stronger increases of the adhesion energy.²⁸

Kelvin Probe Analysis. In addition to XPS depth profiling, Kelvin probe analysis was carried out of the fractured samples (Figure 5). Due to measurement constraints, only electrically conductive samples could be examined, meaning that only the metal side of the samples that fractured at the BHJ/HTL interface could be measured, i.e. all of the unaged samples, and silver-containing samples that had been aged for one week. These measurements showed a significant decline in surface potential with thermal ageing for the silver samples. As the surface potential reflects an ensemble average of the work functions of the materials at the surface of the sample, if the composition of the fractured surface were altered by inter-diffusion, this would be expected to have an effect on the measured surface potential.

The timescale of the increase in fracture energy and diffusion matches that of the early decay in V_{OC} seen in inverted OPV containing a MoO_3 HTL and a silver hole-collecting electrode (Figure 2(a)). This would suggest that these two phenomena are related. In open circuit conditions, charge carrier generation is balanced by recombination.²⁹ V_{OC} loss in OPV can be either related to a decrease of the charge carrier density (with unchanged density of states) due to an increased trap-mediated recombination rate or to a broadening of the density of states (with unchanged carrier density).^{30–32} Both phenomena would result in a decrease of the quasi-Fermi levels splitting and then in a V_{OC} loss.

The presence of contaminants in the BHJ near either electrode can give rise to the formation of trap levels in the band gap.^{33,34} These charge traps would have the effect of increasing the recombination rate via trap-assisted recombination, in which one charge carrier is held in the trap level until it recombines by collision with the opposite charge carrier, decreasing the V_{OC} .^{35,36} It is therefore possible that the diffusion of metallic elements into the BHJ could lead to V_{OC} loss via charge trap formation. Inter-diffusion of the BHJ, HTL and electrode layers

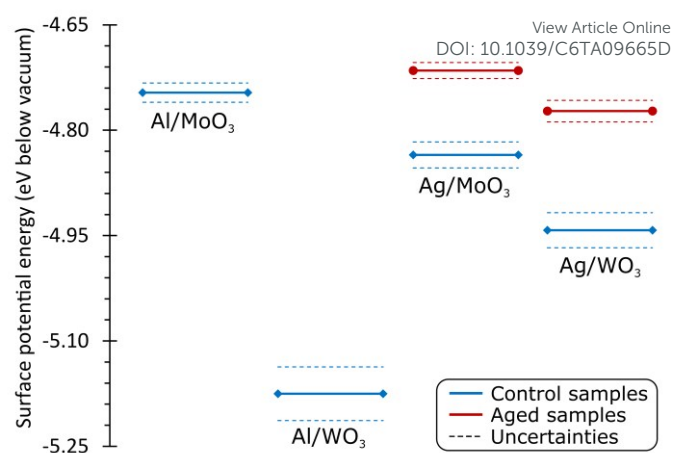


Figure 5: Kelvin probe analysis of the fractured samples. Note that only samples that fractured at the HTL/BHJ boundary could be analysed. The levels in blue (diamonds) correspond to the un-aged samples, while those in red (circles) correspond to samples with silver electrodes that had been aged one week. In all cases the metal side is analysed. Uncertainties (dashed lines) represent a standard error when averaged across 50 measurements.

has been demonstrated in this study in devices which incorporate silver electrodes and either WO_3 or MoO_3 HTLs. Inter-diffusion has also been demonstrated previously with the combination of silver and PEDOT:PSS.^{37,38} However, it is only in the combination of silver and MoO_3 that V_{OC} loss is observed, it is not observed if an aluminium electrode, WO_3 HTL, or PEDOT:PSS HTL are used.¹⁵ This implies that an additional chemical interaction with or between the diffused species must occur for the formation of trap levels, and here that interaction only takes place between silver and MoO_3 .

PCDTBT:PC₇₁BM Thermal ageing behaviour. In order to determine if the two different degradation mechanisms identified in P3HT:PCBM solar cells also occur in other donor:acceptor active layers, a thermal degradation study was carried out on inverted OPV devices with PCDTBT:PC₇₁BM active layers, MoO_3 HTLs and either silver or aluminium top electrodes. The devices exhibit initial performances between 5 and 5.2% regardless of the top electrode (ESI, Table S1). These devices showed much greater thermal stability than their P3HT:PC₆₁BM counterparts (Figure 6), exhibiting little or no long-term loss of efficiency with thermal ageing after an initial decline. This greater stability, is largely a consequence of a greatly reduced decline in J_{SC} (Figure S1 in the ESI) which, unlike the P3HT:PC₆₁BM devices, exhibit high stability after the early stages of the experiment. The high degree of thermal stability of OPV devices containing PCDTBT:PC₇₁BM active layers is typically attributed to the high glass transition point (T_g) of PCDTBT, which means that at typical testing temperatures donor/acceptor domain growth (which is the origin of the J_{SC} loss in P3HT devices) in a BHJ containing PCDTBT is inhibited by the poorer mass transport.^{39,40} Interestingly, the V_{OC} loss only observed for P3HT:PC₆₁BM with MoO_3/Ag top electrode (Figure 1a), is also observed in PCDTBT:PC₇₁BM solar cells, but on a longer timescale. The difference in mass transport in the BHJ between the two different active layers would also be expected to have an effect

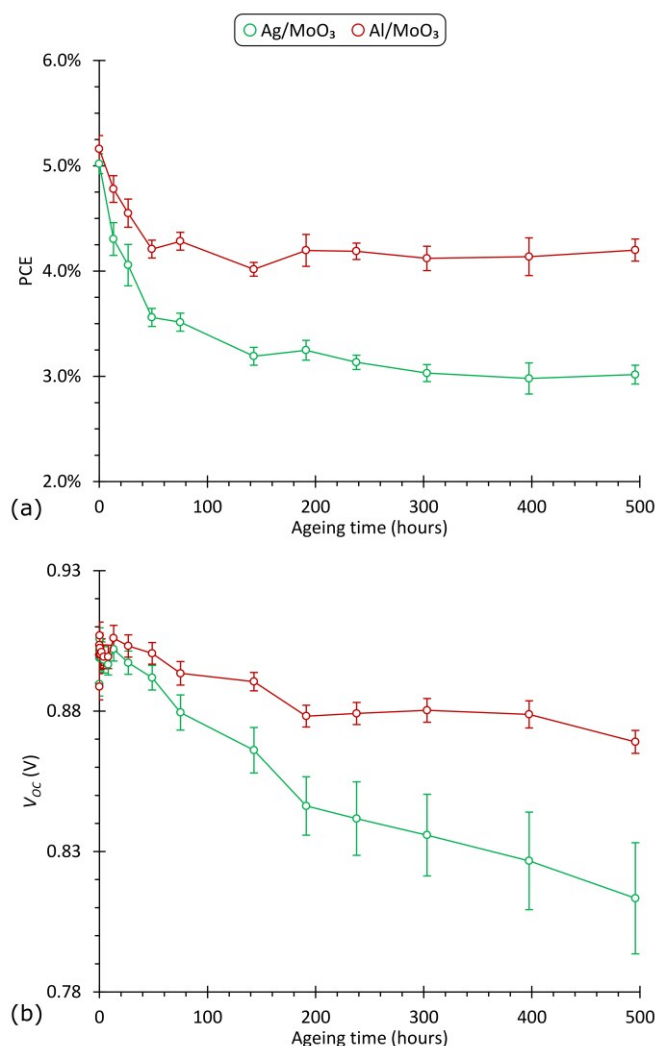


Figure 6: The evolution of the PCE (a), and V_{oc} (b) of the PCDTBT:PC₇₁BM inverted OPV devices with thermal ageing in the dark in an inert atmosphere. The devices have MoO₃ HTLs and either aluminium or silver top electrodes. The uncertainties represent one standard deviation when averaged across 12 devices.

on any other diffusion-driven degradation mechanisms that might be present in the device, such as the one proposed to give rise to the V_{oc} loss in the P3HT:PC₆₁BM/MoO₃/Ag devices (Figure 2a). It is evident from Figure 6 that there is a decline in the V_{oc} of the PCDTBT:PC₇₁BM/MoO₃/Ag devices, that this decline is much greater when a silver electrode is used in conjunction with a MoO₃ HTL, and that it proceeds much more slowly than the V_{oc} loss observed with their P3HT:PC₆₀BM counterparts. The V_{oc} loss may arise from the same diffusion mechanism with both active layers (as is suggested by the material selectivity) and the slowing of the loss should only be due to the inhibition of mass transport by the higher T_g polymer. As a result, by inhibiting the two different degradation mechanisms, phase segregation on the one hand, and silver diffusion on the other hand, a thermally stable architecture based on PCDTBT:PC₇₁BM and MoO₃/Al top electrode was developed which exhibited only a 15% efficiency loss after 500 h of thermal ageing.

Conclusions

View Article Online

DOI: 10.1039/C6TA09665D

This study has examined the mechanical stability of thermally-aged inverted OPV devices incorporating metal oxide HTLs using fracture analysis. It was found that in all cases the fracture path eventually moved into the BHJ layer, a consequence of phase segregation-induced weakening of the active layer simultaneously with a strengthening of the interface. The weakening of the active layer is correlated to J_{sc} loss observed in studies of thermal ageing of OPV devices. XPS depth profiling was used to probe the origins of the interfacial strengthening, demonstrating that inter-diffusion at the hole-extraction interface occurs in silver-containing samples. This is the likely cause of the V_{oc} loss observed in the thermal ageing of silver-molybdenum oxide OPV devices through the formation of charge traps and subsequent increase in the recombination rate. Replacement of silver top electrode with an aluminium one leads to an improvement of the thermal stability of OPV devices for different donor:acceptor combinations (P3HT:PCBM and PCDTBT:PC₇₁BM). These findings can be used to further inform the design and choice of materials in the development of OPV solar cells.

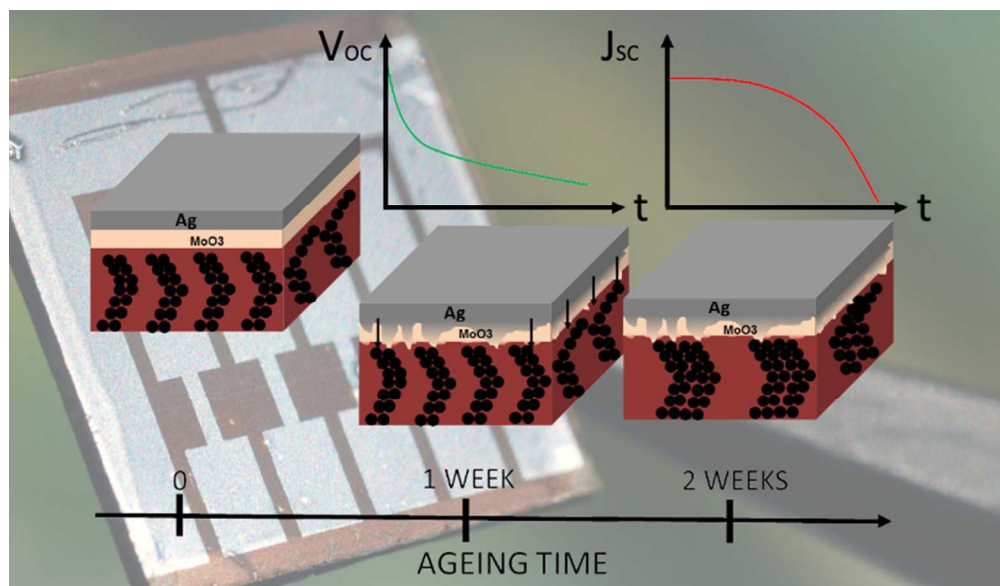
Acknowledgements

This work was carried out as a part of a collaboration between the IMS Laboratory (*Le laboratoire de l'Intégration du Matériau au Système* – CNRS UMR5218) at the University of Bordeaux, and the Department of Materials Science at Stanford University. The authors would like to thank the McGehee Group at Stanford University for the use of their facilities during sample preparation. This work was financially supported by the French National Research Agency (*Agence Nationale de la Recherche*) in the frame of the Project Nos. ANR-13-JS09-0014-01 “IN-STEP” and ANR-13-PRGE-0006 “HELIOS.” WG was financed to travel to the United States by LabEx AMADEus (ANR-10-LABX-42) in the framework of IdEx Bordeaux (ANR-10-IDEX-03-02) – the *Investissements d'Avenir* programme of the French Government, managed by the French National Research Agency (*Agence Nationale de la Recherche*). Part of this work was performed at the Stanford Nano Shared Facilities (SNSF).

Notes and references

- 1 F. C. Krebs, N. Espinosa, M. Hösel, R. R. Søndergaard and M. Jørgensen, *Adv. Mater.*, 2014, **26**, 29–39.
- 2 N. Espinosa, F. O. Lenzmann, S. Ryley, D. Angmo, M. Hösel, R. R. Søndergaard, D. Huss, S. Däfinger, S. Gritsch, J. M. Kroon, M. Jørgensen and F. C. Krebs, *J. Mater. Chem. A*, 2013, **1**, 7037.
- 3 C. W. Tang, *Appl. Phys. Lett.*, 1986, **48**, 183.
- 4 J. Zhao, Y. Li, G. Yang, K. Jiang, H. Lin, H. Ade, W. Ma and H. Yan, *Nat. Energy*, 2016, **1**, 15027.
- 5 M. A. Green, K. Emery, Y. Hishikawa, W. Warta and E. D. Dunlop, *Prog. Photovoltaics Res. Appl.*, 2016, **24**, 3–11.
- 6 M. Hösel, H. F. Dam and F. C. Krebs, *Energy Technol.*, 2015, **3**, 293–304.

- 7 S. Berny, N. Blouin, A. Distler, H.-J. Egelhaaf, M. Krompiec, A. Lohr, O. R. Lozman, G. E. Morse, L. Nanson, A. Pron, T. Sauermann, N. Seidler, S. Tierney, P. Tiwana, M. Wagner and H. Wilson, *Adv. Sci.*, 2016, **3**, 1500342.
- 8 Z. George, E. Voroshazi, C. Lindqvist, R. Kroon, W. Zhuang, E. Wang, P. Henriksson, A. Hadipour and M. R. Andersson, *Sol. Energy Mater. Sol. Cells*, 2015, **133**, 99–104.
- 9 M. Jørgensen, K. Norrman and F. C. Krebs, *Sol. Energy Mater. Sol. Cells*, 2008, **92**, 686–714.
- 10 S. Züfle, M. T. Neukom, S. Altazin, M. Zinggeler, M. Chrapa, T. Offermans and B. Ruhstaller, *Adv. Energy Mater.*, 2015, **5**, 1500835.
- 11 E. Voroshazi, B. Verreet, A. Buri, R. Müller, D. Di Nuzzo and P. Heremans, *Org. Electron.*, 2011, **12**, 736–744.
- 12 M. S. White, D. C. Olson, S. E. Shaheen, N. Kopidakis and D. S. Ginley, *Appl. Phys. Lett.*, 2006, **89**, 143517.
- 13 Y. Şahin, S. Alem, R. De Bettignies and J. M. Nunzi, *Thin Solid Films*, 2005, **476**, 340–343.
- 14 G. Li, C. W. Chu, V. Shrotriya, J. Huang and Y. Yang, *Appl. Phys. Lett.*, 2006, **88**, 3–6.
- 15 W. Greenbank, L. Hirsch, G. Wantz and S. Chambon, *Appl. Phys. Lett.*, 2015, **107**, 263301.
- 16 M. Lin, Y. Huang, C. Yen, C. Tsao and Y. Yen, *Polym. Degrad. Stab.*, 2016, **134**, 245–250.
- 17 T. L. Anderson, *Fracture mechanics: fundamentals and applications*, CRC press, 3rd edn., 2005.
- 18 M. O. Reese, S. a. Gevorgyan, M. Jørgensen, E. Bundgaard, S. R. Kurtz, D. S. Ginley, D. C. Olson, M. T. Lloyd, P. Morvillo, E. a. Katz, A. Elschner, O. Haillant, T. R. Currier, V. Shrotriya, M. Hermenau, M. Riede, K. R. Kirov, G. Trimmel, T. Rath, O. Inganäs, F. Zhang, M. Andersson, K. Tvingstedt, M. Lira-Cantu, D. Laird, C. McGuinness, S. (Jimmy) Gowrisanker, M. Pannone, M. Xiao, J. Hauch, R. Steim, D. M. DeLongchamp, R. Rösch, H. Hoppe, N. Espinosa, A. Urbina, G. Yaman-Uzunoglu, J.-B. Bonekamp, A. J. J. M. van Breemen, C. Girotto, E. Voroshazi and F. C. Krebs, *Sol. Energy Mater. Sol. Cells*, 2011, **95**, 1253–1267.
- 19 M. F. Kanninen, *Int. J. Fract.*, 1973, **9**, 83–92.
- 20 V. Palermo, M. Palma, Ž. Tomović, M. D. Watson, R. Friedlein, K. Müllen and P. Samorì, *ChemPhysChem*, 2005, **6**, 2371–2375.
- 21 C. Sommerhalter, T. W. Matthes, T. Glatzel, A. Jäger-Waldau and M. C. Lux-Steiner, *Appl. Phys. Lett.*, 1999, **75**, 286.
- 22 V. Brand, C. Bruner and R. H. Dauskardt, *Sol. Energy Mater. Sol. Cells*, 2012, **99**, 182–189.
- 23 S. R. Dupont, E. Voroshazi, D. Nordlund and R. H. Dauskardt, *Sol. Energy Mater. Sol. Cells*, 2015, **132**, 443–449.
- 24 S. R. Dupont, M. Oliver, F. C. Krebs and R. H. Dauskardt, *Sol. Energy Mater. Sol. Cells*, 2012, **97**, 171–175.
- 25 S. R. Dupont, E. Voroshazi, P. Heremans and R. H. Dauskardt, *Org. Electron.*, 2013, **14**, 1262–1270.
- 26 V. Balcaen, N. Rolston, S. R. Dupont, E. Voroshazi and R. H. Dauskardt, *Sol. Energy Mater. Sol. Cells*, 2015, **143**, 418–423.
- 27 N. R. Tummala, C. Bruner, C. Risko, J.-L. Brédas and R. H. Dauskardt, *ACS Appl. Mater. Interfaces*, 2015, **7**, 9957–9964.
- 28 M. Corazza, N. Rolston, R. H. Dauskardt, M. Beliatas, F. C. Krebs and S. A. Gevorgyan, *Adv. Energy Mater.*, 2016, **6**, 1501927.
- 29 A. K. Thakur, G. Wantz, G. Garcia-Belmonte, J. Bisquert and L. Hirsch, *Sol. Energy Mater. Sol. Cells*, 2011, **95**, 2131–2135.
- 30 E. Voroshazi, I. Cardinaletti, T. Conard and B. P. Rand, *Adv. Energy Mater.*, 2014, **4**, 1400848. DOI: 10.1039/C6TA09665D
- 31 T. Heumueller, T. M. Burke, W. R. Mateker, I. T. Sachs-Quintana, K. Vandewal, C. J. Brabec and M. D. McGehee, *Adv. Energy Mater.*, 2015, **5**, 1500111.
- 32 A. K. Thakur, H. Baboz, G. Wantz, J. Hodgkiss and L. Hirsch, *J. Appl. Phys.*, 2012, **112**, 44502.
- 33 C. M. Proctor, M. Kuik and T.-Q. Nguyen, *Prog. Polym. Sci.*, 2013, **38**, 1941–1960.
- 34 L. Kaake, X.-D. Dang, W. L. Leong, Y. Zhang, A. Heeger and T.-Q. Nguyen, *Adv. Mater.*, 2013, **25**, 1706–1712.
- 35 S. R. Cowan, A. Roy and A. J. Heeger, *Phys. Rev. B*, 2010, **82**, 245207.
- 36 C. H. Peters, I. T. Sachs-Quintana, W. R. Mateker, T. Heumueller, J. Rivnay, R. Noriega, Z. M. Beiley, E. T. Hoke, A. Salleo and M. D. McGehee, *Adv. Mater.*, 2012, **24**, 663–668.
- 37 Y. Suh, N. Lu, S. H. Lee, W.-S. Chung, K. Kim, B. Kim, M. J. Ko and M. J. Kim, *ACS Appl. Mater. Interfaces*, 2012, **4**, 5118–24.
- 38 S. R. Dupont, F. Novoa, E. Voroshazi and R. H. Dauskardt, *Adv. Funct. Mater.*, 2014, **24**, 1325–1332.
- 39 P. A. Staniec, A. J. Parnell, A. D. F. Dunbar, H. Yi, A. J. Pearson, T. Wang, P. E. Hopkinson, C. Kinane, R. M. Dalglish, A. M. Donald, A. J. Ryan, A. Iraqi, R. A. L. Jones and D. G. Lidzey, *Adv. Energy Mater.*, 2011, **1**, 499–504.
- 40 S. Cho, J. H. Seo, S. H. Park, S. Beaupré, M. Leclerc and A. J. Heeger, *Adv. Mater.*, 2010, **22**, 1253–1257.



68x39mm (300 x 300 DPI)